J. Fluid Mech. (2008), *vol.* 596, *pp.* 49–72.
doi:10.1017/S0022112007008956 Printed in the United Kingdom

Sting-free measurements on a magnetically supported right circular cylinder aligned with the free stream

HIROSHI HIGUCHI[1], HIDEO SAWADA[2] AND HIROYUKI KATO[2]

[1]Syracuse University, Syracuse, NY 13244, USA

[2]Japan Aerospace Exploration Agency, Chofu, Tokyo 182-8522, Japan

(Received 25 August 2006 and in revised form 24 August 2007)

The flow over cylinders of varying fineness ratio (length to diameter) aligned with the free stream was examined using a magnetic suspension and balance system in order to avoid model support interference. The drag coefficient variation of a right circular cylinder was obtained for a wide range of fineness ratios. Particle image velocimetry (PIV) was used to examine the flow field, particularly the behaviour of the leading-edge separation shear layer and its effect on the wake. Reynolds numbers based on the cylinder diameter ranged from 5×10^4 to 1.1×10^5, while the major portion of the experiment was conducted at $Re_D = 1.0 \times 10^5$. For moderately large fineness ratio, the shear layer reattaches with subsequent growth of the boundary layer, whereas over shorter cylinders, the shear layer remains detached. Differences in the wake recirculation region and the immediate wake patterns are clarified in terms of both the mean velocity and turbulent flow fields, including longitudinal vortical structures in the cross-flow plane of the wake. The minimum drag corresponded to the fineness ratio for which the separated shear layer reattached at the trailing edge of the cylinder. The base pressure was obtained with a telemetry technique. Pressure fields and aerodynamic force fluctuations are also discussed.

1. Introduction

Axial flow along a circular cylinder represents a canonical configuration that is applicable to aircraft fuselages, missiles, road vehicles, etc. Drag coefficients of the cylinder aligned with the flow are listed in various handbooks and textbooks (see, e.g., Blevins 1984; Crowe, Elger & Roberson 2005). Blevins quotes Nakaguchi (1978) but the original source dates back to Hoerner (1958) who in turn quoted Eiffel's experiments (1907, 1913). The Eiffel tower was used in the 1907 experiment in which various models were dropped along a guide cable. Eiffel repeated the experiment in a low-speed wind tunnel in 1913. While some additional drag measurements were conducted by Roberson *et al.* (1972), no modern systematic measurements are available for this configuration and the classical data may be subject to interference from sting-mounted drag balances. In this investigation, we re-examine the flow over this very well-defined geometry, with the key parameters being the length-to-diameter ratio (fineness ratio) and the Reynolds number. Here the term fineness ratio is adopted, see Hoerner (1958), though other terms such as slenderness ratio or aspect ratio may be as applicable. The resulting flow field is complicated and involves a

shear layer separated from the sharp leading edges that may or may not reattach at a given fineness ratio, ultimately affecting the subsequent boundary layer development. At the end of the cylinder, the boundary layer separates from the trailing edge and is followed by a recirculation region and three-dimensional wake structure.

Since the flows about the front face, in the boundary layer and in the wake of the axisymmetric body are all critical to accurately determining the drag coefficient, the traditional model support poses certain difficulties. In order to avoid any interference from model sting or other support, the present experiment utilized the Magnetic Suspension and Balance System at the Institute of Space Technology and Aeronautics, Japan Aerospace Exploration Agency. Precise model alignment is easily implemented, and the instantaneous forces and moment acting on the entire body are directly measured as a part of a feedback control system. This approach avoids the introduction of unnecessary interference or flow disturbance due to a conventional force balance. A new more definitive data set of drag coefficients over a wide range of fineness ratio has been obtained, and the effect of the shear layer reattachment has been investigated in further detail with the flow field measurements.

The phenomenon of flow separation from the shoulder of the cylinder and its reattachment was studied by Kiya *et al.* (1991) who found a cellular structure in the reattachment region. Their models were supported from downstream. In a typical laboratory setup, however, due to the necessity of supporting the model with wires or a sting, the leading-edge shear layer and the wake, as well as the interaction between them, are difficult to observe simultaneously.

In our recent study using a water channel and the particle image velocimetry (PIV) system, the flow structures of the separating and reattaching shear layer and of the wake behind a sting-mounted cylinder were examined (Higuchi *et al.* 2006). The wake of a supporting strut was found to influence the cross-sectional mean velocity profile downstream, and a disturbance from upstream was detectable in the instantaneous velocity field. A snapshot proper orthogonal decomposition (POD) revealed two symmetrical pairs of counter-rotating longitudinal vortex structures which were deemed to be a part of the intrinsic flow field, though the first mode clearly showed the support interference.

Therefore, in order to avoid any such interference of the support on flow field measurements, the present study employed PIV in conjunction with a magnetically suspended model. There have been studies on magnetically supported models in the past (e.g. Judd, Vlanjinac & Covert 1971), but the experiments were restricted to mean drag force measurements because the limited model size and instrumentation techniques were not appropriate for this type of unsteady separated flow. Here, modern digital PIV was incorporated for velocity field measurement without interference from the model support and the base pressure was measured using a telemetry system.

2. Description of experiment and set-up

2.1. *Magnetic model suspension, force balance and wind tunnel*

The experiment was conducted using the Magnetic Suspension and Balance System at the Institute of Space Technology and Aeronautics, Japan Aerospace Exploration Agency (JAXA). The system was developed by Sawada and his group (Sawada & Kunimasu 2001). Figure 1 shows schematically the coil (or electromagnet) arrangement used in the system, and the specifications of the individual coils are listed in table 1. Here, the colloquial term, coil, is used as it appeared in the reference above. This particular figure is for a smaller prototype, but the arrangement is

Coil	Turn number	Size	Purpose
0,9	50	620×620	drag
1,3,5,7	$97 + 97$	200×200	lift, pitch moment
2,4,6,8	100	200×200	side force, yawing moment, rolling moment
coil drive units	130V, 120A in continuous mode... 3 units 130V, 60A in continuous mode... 4 units		
control	5 DOF for models with a main magnet only 6 DOF for special models with pair magnets		

TABLE 1. Magnetic suspension and balance system coils.

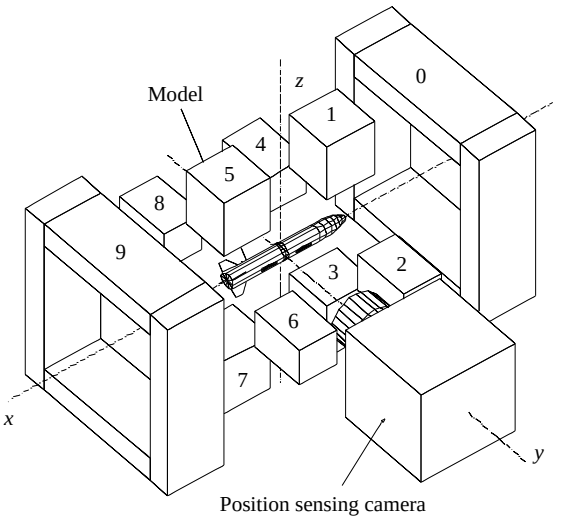

FIGURE 1. Magnetic Support and Balance System arrangement (not to scale, only one camera is shown).

clearly shown. Five pairs of coils provide the necessary control of the model in all directions. The currents to individual coils provide instantaneous drag, lift, side force, and pitching and yawing moments. The model position and attitude were monitored by two CCD cameras oriented orthogonally to each other and controlled at a 245 Hz feedback frequency. Two colours and filters were used to separate reflected light in two directions. The balance system was installed in the subsonic wind tunnel with a 60 cm $\times$ 60 cm test section. Compared to systems reported in the past (Judd *et al.*, 1971), the size of the present magnetic suspension and balance system affords adequate spatial resolution for accurate flow field measurements. The available flow speed ranged from 10 to 35 m s^{-1} with a free-stream turbulence level less than 0.08%. The magnet current was calibrated against a known force applied through pulleys and weights for each model and had a repeatability within 0.2% (Sawada *et al.* 2004). Further detail of the Magnetic Suspension and Balance System and the wind tunnel can be found in Sawada & Kunimasu (2001).

2.2. *Test models*

Each model was made from aluminum alloy and housed inside a rod-shaped or annular permanent magnet, along the centreline. Figure 2 illustrates the cylindrical models supported magnetically in the test section. In addition to the model edges,

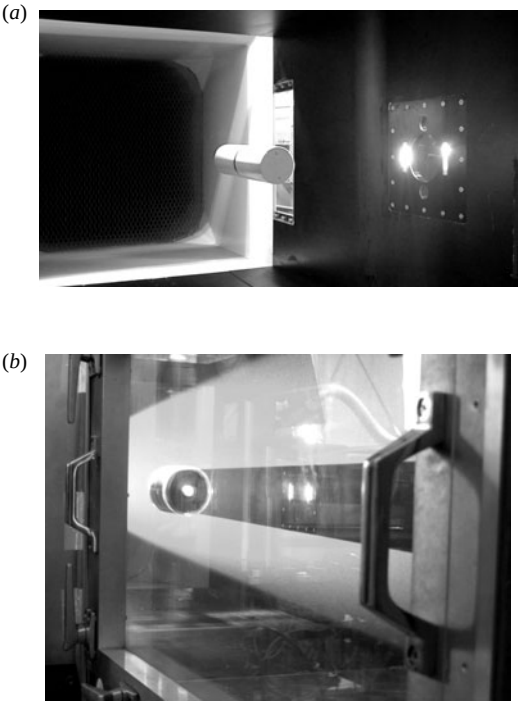

FIGURE 2. (*a*) A magnetically supported 45 mm diameter cylinder model. (*b*) Magnetically suspended cylinder model during the PIV measurement.

the sensing cameras use a vertical stripe, located in the middle, to detect the model position and attitude. In order to provide a wide range of fineness ratios, models with different diameters were used. One was of 45 mm diameter (see figure 2*a*) and the centre section enclosed the permanent magnet. By using end caps of different lengths, nine fineness ratios between 4.13 and 8.13 were achieved. A second model had a diameter of 85 mm and the third 110 mm. These larger diameter models provided a fineness ratio down to 1.272. An additional model of 25 mm diameter and fineness ratio of 6 was also used. The Reynolds number based on the diameter ranged from 5×10^4 to 1.1×10^5. Figure 2(*b*) shows the 110 mm diameter model suspended in the test section illuminated by a pulsed laser sheet during the PIV measurement.

For force measurements, as well as some initial flow measurements using a conventional hot-wire probe and pressure probes, the test models ranged in diameter from 25 mm to 110 mm to provide a wide range of fineness ratios. For the present velocity field measurements with the PIV system described in the next section, the diameter of the model was fixed at 110 mm and two lengths were chosen to provide $L/D = 1.31$ and 1.68. The position was controlled within ± 0.2 mm in any direction and the yaw and pitch angles of the model were held constant within $\pm 0.1^\circ$. Typical instantaneous control current measurements and the model position are shown in figure 3. Sharp pulses in the figures are due to the laser light sheet for the PIV (see figure 2*b*). The base pressure measurements were also conducted with the 110 mm diameter model. Position sensing for these short models needed special care as described in Sawada & Kunimasu (2001). The optical sensing of the model position was not affected by the pulsed laser light sheet applied to measure the velocity field.

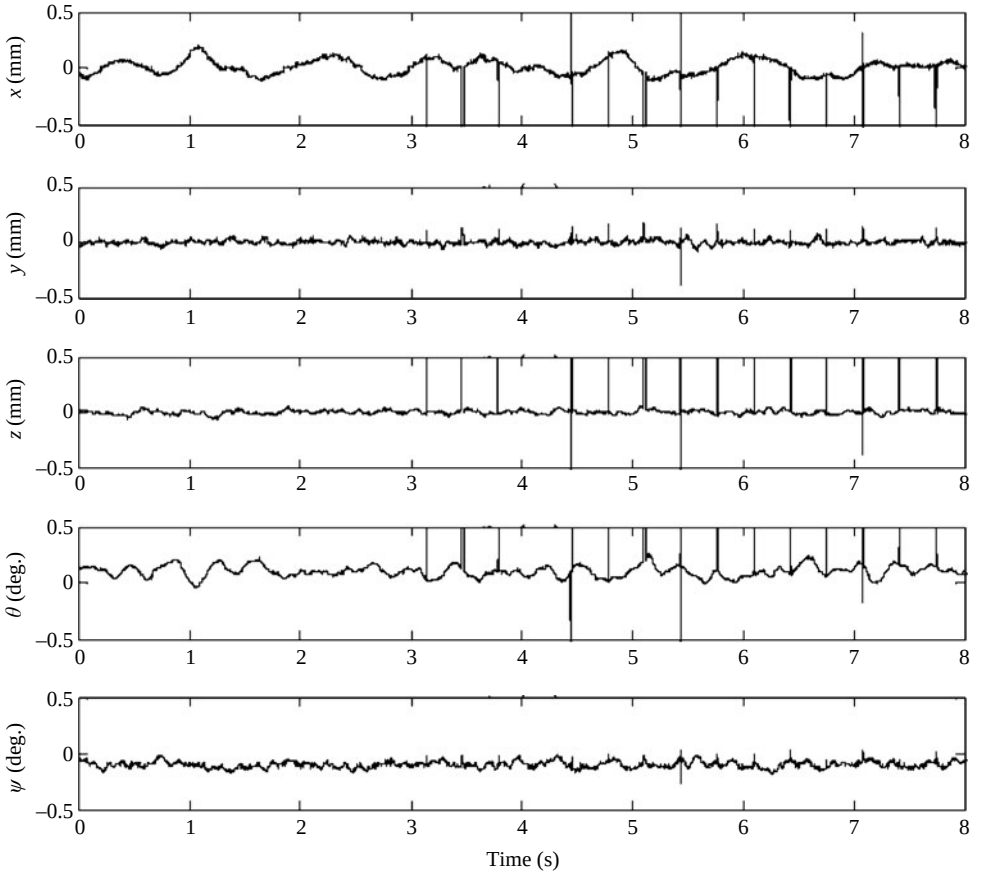

FIGURE 3. Time variation of model position and orientation ($L/D = 1.31$).

Time histories of the position and the coil currents will be discussed in the results section below.

2.3. *Particle image velocimetry (PIV) system set-up*

A two-Component PIV system developed for the JAXA wind tunnels (Watanabe & Kato 2003) was employed for the present experiment. The laser is a two-cavity double-pulse Nd:YAG (Quantel, Twins CFR 200) with maximum pulse energy of 200 mJ/pulse at a repetition rate of 15 Hz. The cross-correlation camera (LaVision, Imager Pro Plus 4M) has a 14-bit monochrome CCD image sensor with 2048×2048 pixels. While the original framing rate of the camera is about 15 Hz, two-component velocity vector maps in the two dimensional PIV measurements are obtained at around 1.5 or 3 Hz, being limited by the data transfer rate to the storage system. The timing between the image acquisition by the CCD camera and the laser pulse was synchronized by a programmable timing unit. Time separation Δt was set between 25 and 95 μs according to the flow speed. Oil droplets with a diameter of around 1 μm were used as the seed particles. In the PIV measurement, the whole flow path of the wind tunnel was seeded by a seeding generator (LG-500) developed by the German Aerospace Center (DLR), with five Laskin nozzles and an impactor plate for generating small seed particles of uniform size. Two PIV set-ups were used in these measurements. In one, the laser light sheet was located perpendicular to the

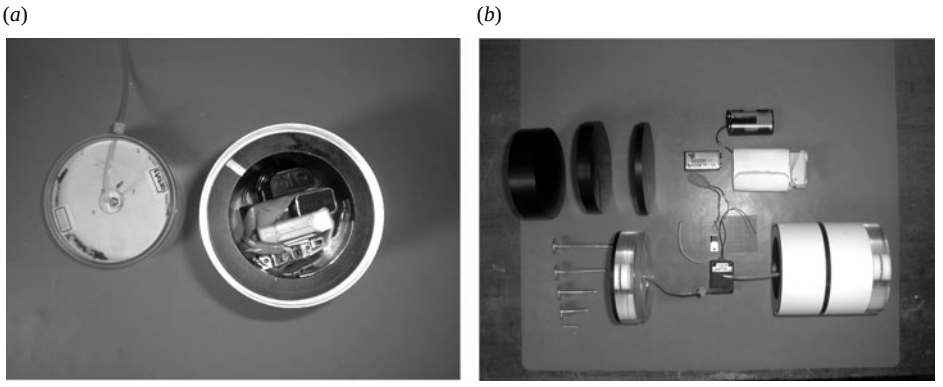

FIGURE 4. Pressure transducer and telemetry system (shows an expanded view. Three plates on the top left are spacers to adjust the fineness ratio.)

free stream. In the other, the laser light sheet was located parallel to the free stream, including the model centre axis (see figure 2*b*). A small mirror was installed in the wind tunnel diffuser because of the limitation of optical access, and a small optical window was created on the diffuser wall for this experiment. In the case of measurements perpendicular to the free stream, the camera was located outside the diffuser and the seeding image was acquired at right angles to the laser light sheet through the mirror. In the case of the measurement plane parallel to the free stream, the laser light sheet was directed upstream by the mirror, and the camera was located along the sidewall of the test section. The size of the PIV measurement region was about 250 mm $\times$ 250 mm in both set-ups. Commercial PIV software (LaVision, DaVis FlowMaster) for acquisition and post processing of the images ran on a PC with 3.06 GHz dual Xeon processors. Typically 2000 pairs of images were captured per run and were stored onto a 6 TB ArrayMasStor L-HP RAID System.

Pairs of particle images acquired by the CCD camera were analysed by means of the fast Fourier transform (FFT)-based cross-correlation technique in the PIV software, resulting in two-component vector maps. In order to achieve sub-pixel accuracy in the vector analysis, Gaussian curve fitting was adopted as the peak search algorithm. The vectors are calculated with 50 % overlap between adjacent interrogation regions. Erroneous vectors were omitted through a peak ratio filter without interpolation for the omitted vectors. Instantaneous data at an identical test condition are ensemble averaged, yielding mean vector maps and profiles. All the instantaneous velocity data are saved for present and future analyses.

2.4. *Base pressure measurement*

Since no support strut or sting is available to transmit pressure measurements or electrical signals, a telemetric system was employed to measure the base pressure on the magnetically suspended models. The electronic pressure transducer, A/D converter and the radio transmitter, as well as a battery to power the unit, were all housed within the test model as shown in figure 4 (Sawada *et al.* 2005). An annular permanent magnet was used to accommodate the instrumentation within the model. The system was specially co-developed by JAXA and NEC Engineering and allows 4-channel simultaneous 12.5 kHz sampling and 12-bit resolution A/D conversion. The digital data were transmitted through a bi-directional wireless LAN method. In addition, it had a 4-bit digital signal source that could be externally controlled. A differential pressure gauge of 500 Pa full scale was housed within the model powered

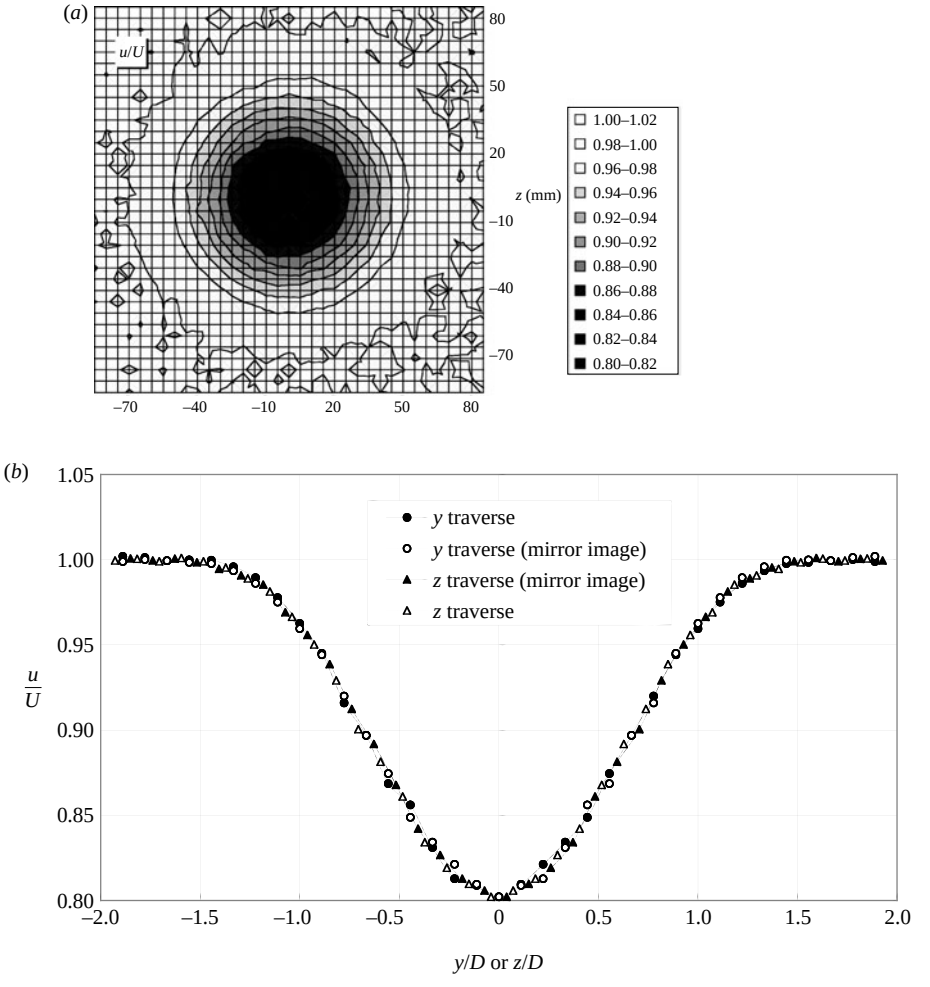

FIGURE 5. Mean axial velocity (u/U) distribution in the wake of the 45 mm diameter cylinder, $L/D = 5.02$ at $x/D = 6.11$ ($Re_D = 1.0 \times 10^5$) (*a*) contour, (*b*) velocity profiles along two axes in the wake.

by a 9 V battery. Two 0.5 mm diameter pressure taps were placed on the cylinder axis at the front and back faces of the model. Figure 4*b* shows the individual components in the assembly. Owing to space limitations, the device was only incorporated into the 110 mm diameter models, i.e. the low fineness ratio range.

3. Results and discussion

3.1. *Initial wake survey behind the magnetically supported cylinder*

Preliminary velocity measurements relied on a more conventional total head probe and a hot-wire probe on two-axis traversing system and the results are limited to regions where the instrumentation was suitable. The mean velocity distribution measured with a pressure probe behind the $L/D = 5.02$ model as presented as a contour map. as well as in both vertical (z) and horizontal (y) directions, see figure 5. The origin of the coordinate system is located at the trailing edge of the model, with the x-component being in the streamwise direction. The mean velocity components

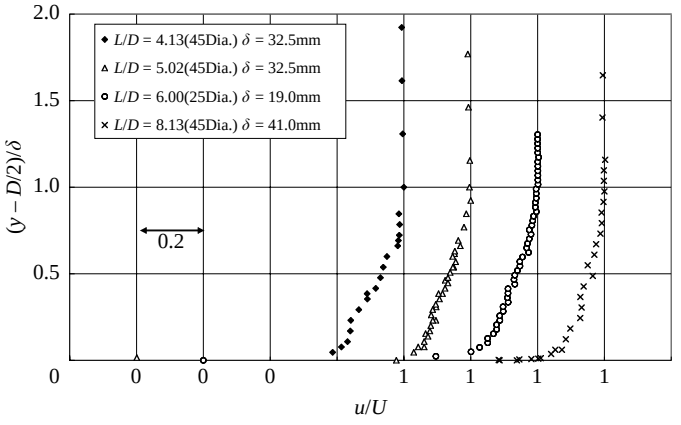

FIGURE 6. Boundary layer profiles at the trailing edge of the model.

(u, v, w) correspond to the (x, y, z) directions, respectively, and U is the free-stream velocity. Figure 5 demonstrates the excellent flow axisymmetry achieved here, clearly benefiting from the absence of the model support. A comparison of the results from PIV measurements behind a sting-mounted model presented by Higuchi *et al.* (2006) and those from PIV measurements with the current magnetic suspension system will be discussed below.

The boundary layer profiles at the trailing edge were measured with a hot-wire probe for various fineness ratios and the mean velocity profiles, normalized by the boundary layer thickness, are shown in figure 6. The Reynolds number was 5×10^4 for the 25 mm cylinder and 1×10^5 for the 45 mm cylinder. Ota (1975) investigated the boundary layer over a sting-mounted sharp-edged cylinder. His velocity profiles, obtained at $x/D = 3.1$, 5.1, and 7.1 from the leading edge, are consistent with the present data at the trailing edge ($L/D = 4.13$–8.13). Ota's experiment corresponded to $Re_D = 5.62 \times 10^4$ and his measurement showed a separation bubble extending from the leading edge and ending with flow reattachment approximately 1.5–1.6 diameters downstream. The mean velocity profiles beyond the reattachment zone indicated a developing turbulent boundary layer. Turbulence intensity profiles are also in general agreement between the two hot-wire measurements, though the present level is somewhat higher. The power spectral density in the immediate wake and shear layers showed the distribution typical of a turbulent boundary layer without a spectral peak. However, at $x/D = 4$, a spectral peak was evident at Strouhal number $St = fD/U = 0.185$, indicative of a helical-mode wake oscillation.

3.2. *Force and base pressure measurements*

As stated earlier, the coil currents needed to hold the model in place provided the lift, drag, and side force, as well as the pitching and yawing moments. The magnetic balance was calibrated against the known weight for each model. The blockage ratio of the model varied between 0.44 % and 2.64 % depending on the model diameter in use. Although the blockage is small, the results shown incorporate the standard blockage correction by Pankhurst & Holder (1952), which was also employed by Judd *et al.* (1971). The correction reduces the drag coefficient by up to 2–3 % for the largest model. Since the instantaneous currents to individual coils were recorded, force–time histories can be analysed, as shown in a later section, once the mass and moment of inertia of each model are known, but here only the time-averaged force has been

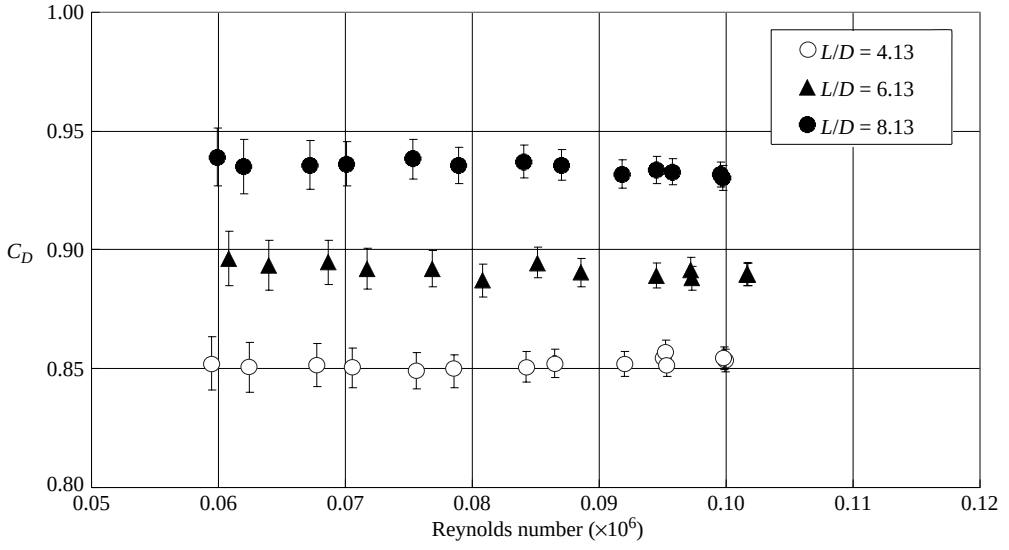

FIGURE 7. Drag coefficient versus Reynolds number for three large fineness ratios.

extracted for all cases. As expected, pitching and yawing moments as well as lift and side forces averaged to be zero and thus only the drag force will be presented and discussed.

Figure 7 shows the measured drag coefficients for the three large fineness ratios over the range of Reynolds number approximately between 6×10^4 and 10^5. The experimental uncertainty is also noted. The Reynolds number dependence as estimated by the empirical skin friction drag for the turbulent boundary layer is not as clearly shown in the measurements, but the expected amount of variation within this Reynolds number range is of the same order as the uncertainty of measurement. For the separation-dominated flow field over the models between $L/D = 1.27$ and 1.79, the Reynolds number dependence on the drag coefficient was negligible. On the other hand, the fineness ratio had a clear influence on the total drag coefficient, as shown at the top of figure 8 for $Re = 10^5$. The measured drag data at $Re = 6 \times 10^4$ are also included. In order to estimate the individual contributions to the total drag, figure 8 shows the momentum loss based on the boundary layer measurements shown in figure 6, and the estimated skin friction drag as well as the total drag. The skin friction was estimated from the empirical power-law formula for a flat-plate turbulent boundary layer (see e.g. Schlichting 1968). The skin friction drag varies as the 1/5th power of Reynolds number based on the length, and thus is proportional to the product of $Re^{-1/5}$ and $(L/D)^{4/5}$. Here, the separated flow at the front corner is considered to attach at 1.5 diameters downstream (Higuchi *et al.* 2006) and thus the effective length has been reduced accordingly. A similar trend is seen among all three curves. As indicated in the figure, the difference between top two lines is, in effect, the base pressure, and that between the bottom two lines corresponds to the pressure drag on the front face. In both cases, they are nearly independent of the fineness ratio.

The base pressure was measured for short cylinders between $L/D = 1.27$ and 1.79 concurrently with the total drag measurement and the results are given in figure 9 for $Re = 10^5$. The base pressure behind the $L/D = 1.27$ and 1.35 cylinders increased slightly with Reynolds number within the range $5 \times 10^4 \sim 10^5$, while the model with

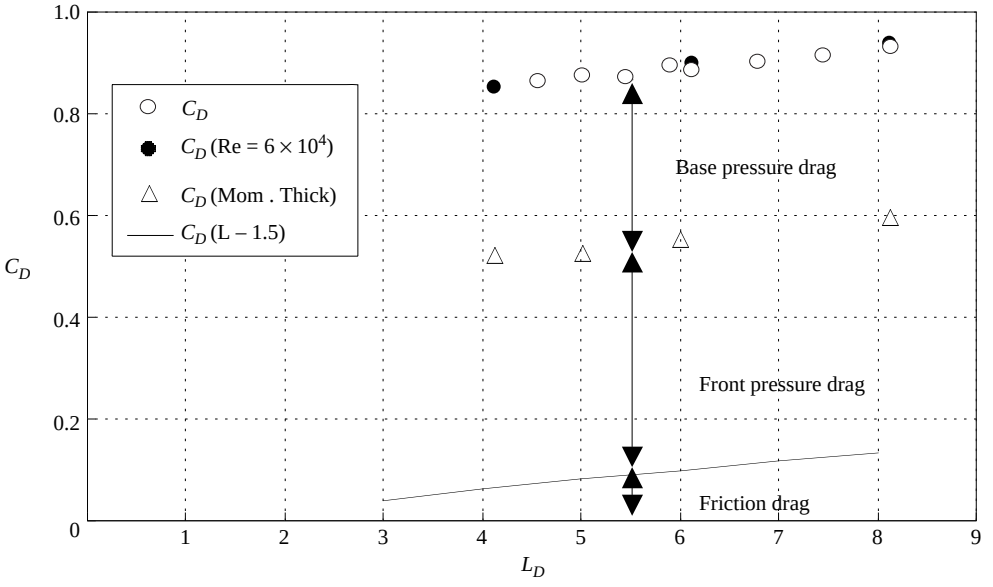

FIGURE 8. Drag coefficient versus fineness ratio ($L/D > 4$). The drag coefficient based on momemtum thickness is also shown. $Re = 1.0 \times 10^5$.

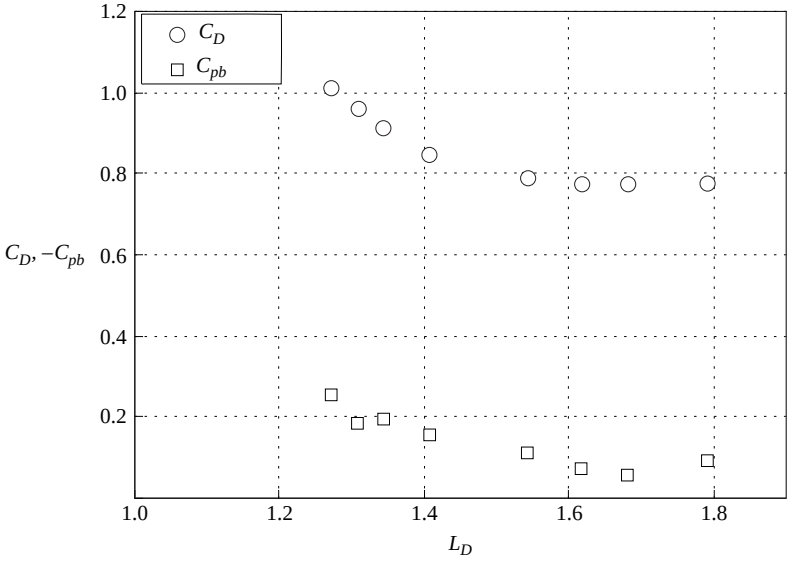

FIGURE 9. Direct base pressure measurement and total drag coefficient at low fineness ratios.

$L/D = 1.79$ exhibited almost constant base pressure within this range. The leading-edge shear layer presumably remained detached at the lower fineness ratio, so the Reynolds number dependence may be attributable to the change in radial width of the separated shear layer region and wake vortex roll-up. In figure 9, it can be seen that for cylinders of small fineness ratio, the variation in total drag is due to changes in base pressure since the front pressure is expected to be unchanged amongst the models and the separated shear layer remains detached (presuming the reverse wall shear stress is small). Both the measured base drag at low fineness ratios

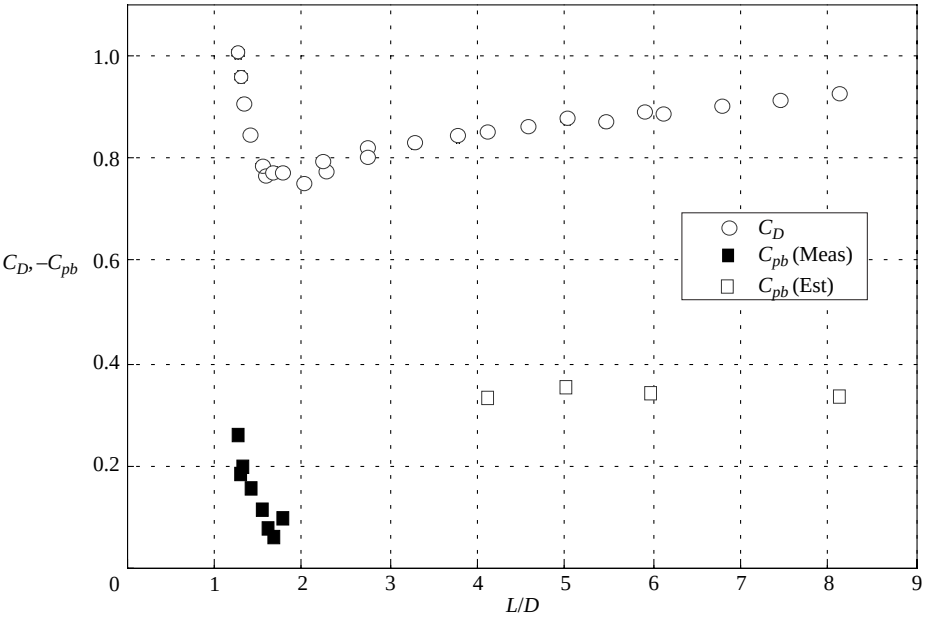

FIGURE 10. Measured and estimated base pressure and the total drag coefficient.

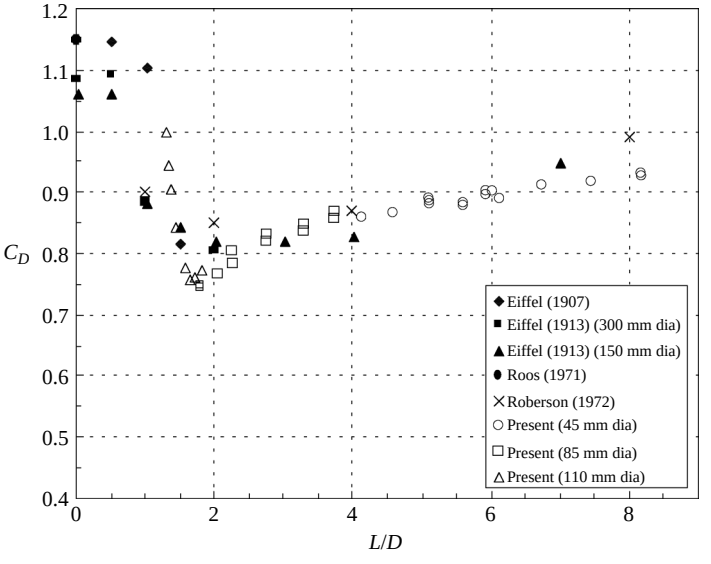

FIGURE 11. Summary of drag coefficient variation with fineness ratio.

and the estimated base drag in figure 9 are plotted together in figure 10 to contrast the variations between the short and long cylinders. The base pressure of the long cylinder is nearly constant whereas the base pressure depends strongly on the fineness ratio for the short cylinder.

Finally, all of the present drag measurements are summarized in figure 11, for $Re_D = 10^5$. The uncertainty in the drag coefficient is about ± 0.5–2 % (larger uncertainty for $L/D < 2$). Previous and historical data are also included. The first

drop experiment by Eiffel (1907) was at a Reynolds number estimated to be between 5.5×10^5 and 1.1×10^6. The second set of Eiffel data (1913) was collected in a wind tunnel with the models cable-mounted in the test section. The experiment pre-dates listing of Reynolds number but is estimated to be nominally in the $1 \times 10^5 \quad \sim 2 \times 10^5$ range. Apparently Hoerner (1958) used Eiffel's second data set (not as listed in his book) and subtracted the estimated skin friction and presented the data in figure 21, Chapter 3 of his book. These values have been quoted for decades in many articles, reference books and textbooks, not necessarily after critical evaluation. Roos & Willmarth (1971) measured the drag coefficients of sphere and disk over a very wide range of the Reynolds number, and their result for the disk as a limiting case of $L/D = 0$ is shown for $Re = 6.04 \times 10^4$, the highest Reynolds number they reported. Roberson *et al.* (1972) carried out wind tunnel measurements on cylinders to study the effect of the high free-stream turbulence, and the data in their data in figure 11 correspond to the Reynolds number of 4×10^4 without grid turbulence imposed.

There is significant scatter in the earlier data for the very low L/D range. It is known that the drag coefficient of a two-dimensional rectangular cylinder reaches the maximum value when the fineness ratio is approximately 0.6, owing to the interaction between the wake vortices and the model base (Bearman & Trueman; 1972, Park & Higuchi 1989; Ohya 1994). Helical vortex formation downstream of the axisymmetric model is expected to produce substantially different interactions with the base plane. Unfortunately, as currently configured, the present magnetic suspension system did not allow experiments at extremely low L/D ratios due to the housing of the magnet and model alignment. This issue will be addressed in future investigations. Nevertheless, the present series of experiments is expected to provide more accurate results for the drag coefficient and to yield an improved understanding of how the drag and the flow of field vary over a wide range of fineness ratio.

3.3. *Flow field measurement*

3.3.1. *Velocity field*

In the previous water channel experiment with sting-mounted models (Higuchi *et al.* 2006), the flow visualization and the PIV measurements were conducted at $L/D = 0.67$, 1.5 and 3 at a lower Reynolds number range of 10^4–3×10^4. The mean flow results revealed that the separated shear layer from the leading edge remained detached for $L/D = 0.67$, reattached almost at the rear corner of the $L/D = 1.5$ model, and reattached approximately 1.5 diameters downstream of the leading edge of the $L/D = 3$ model causing a well-defined recirculation bubble (see figure 2 in that reference). This recirculation bubble, with almost the longitudinal extent of the cylinder, causes the drag coefficient to exhibit a minimum value as shown in figure 11. Thus the sting-free velocity field measurement with the PIV technique was performed focusing on two fineness ratios, $L/D = 1.31$ and 1.68. Both the streamwise cross-sectional plane and the azimuthal plane normal to the free stream were examined. The test model in the wind tunnel in the presence of the laser light sheet for the present PIV measurement was shown in figure 2(*b*).

Each pair of PIV images produces a snapshot of the velocity field. Figure 12(*a*) shows the instantaneous velocity vector field over the magnetically suspended $L/D = 1.31$ model. The Reynolds number is kept at 10^5. It is apparent that large vortices form along the shear layer separated from the leading edge. Except for the initial shear layer up to the midpoint of the model, the unsteady velocity field is highly asymmetric as indicated by the differences between the top and the bottom shear layers in the figure. The shear layer develops downstream without attachment to the

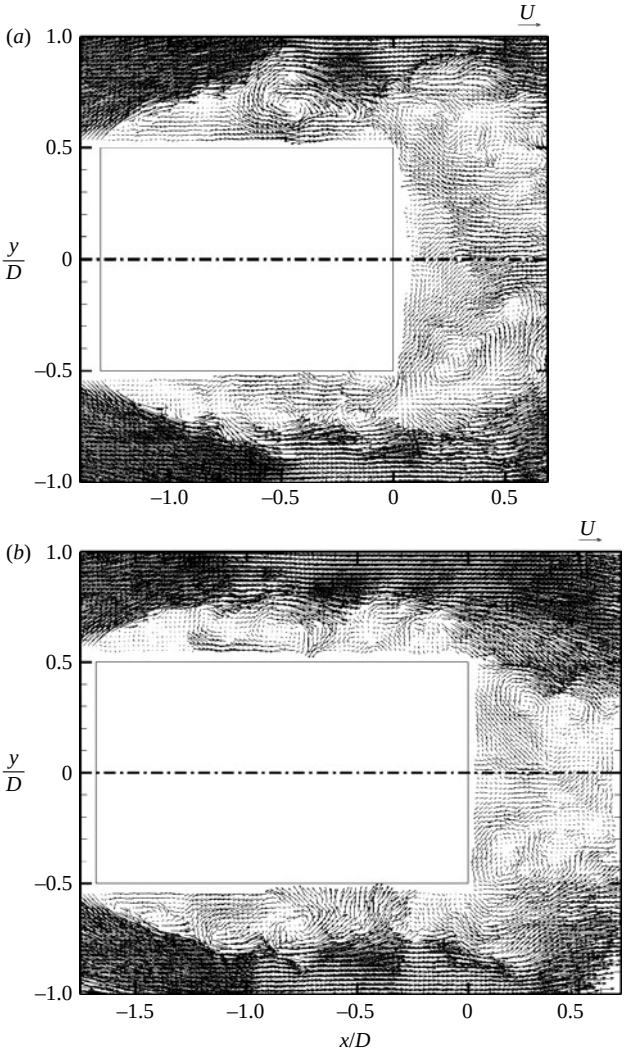

FIGURE 12. Instantaneous velocity vector field ($Re_D = 1.0 \times 10^5$): (*a*) $L/D = 1.31$, (*b*) $L/D = 1.68$.

wall and starts forming a large-scale wake vortex. The instantaneous velocity vector field in figure 12(*b*) reveals similar shear layer roll-up for $L/D = 1.68$. However, the vortex structure in the separating shear layer is smaller and the vortices are seen to impinge on the wall near the end of the cylinder, and here the magnitude of instantaneous velocity is reduced along with the wake structure. The unsteady vortical structures will be discussed further in the next section.

Figure 13(*a*) shows the mean velocity field over the $L/D = 1.31$ model and figure 13(*b*), that over the $L/D = 1.68$ model. Here, the statistical quantities were obtained by ensemble-averaging 2000 consecutive snapshots. Naturally, the frame rate was too slow to resolve individual shedding cycles. The shear layer reattachment can be observed just before the trailing edge of the latter model, consistent with the reattachment point measured by Higuchi *et al.* (2006) on a longer $L/D = 3$ model at $Re_D = 10^4$.

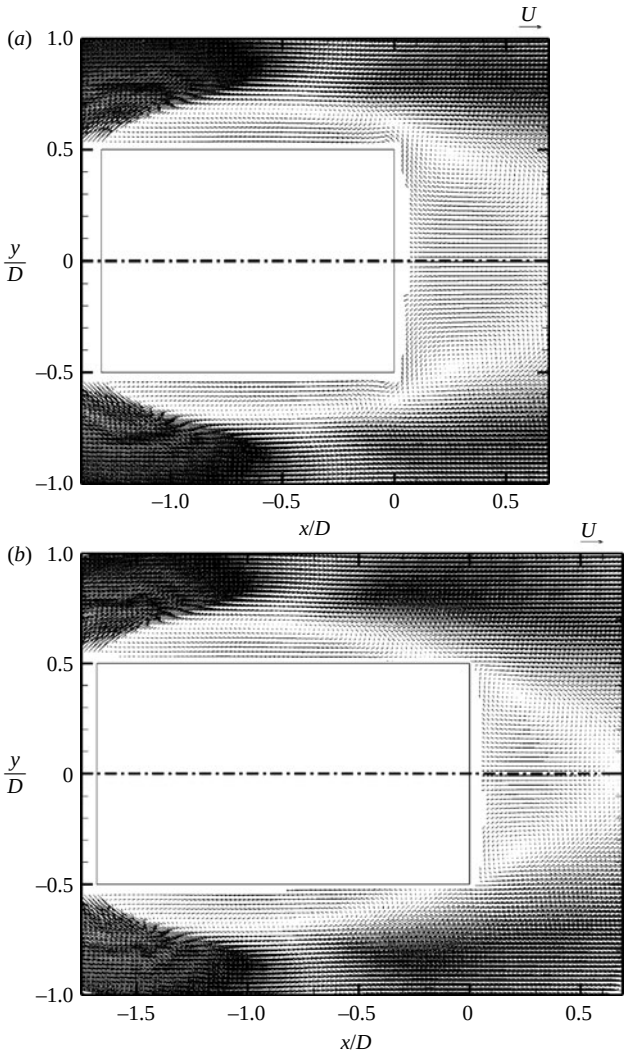

FIGURE 13. Mean velocity vector field ($Re_D = 1.0 \times 10^5$): (*a*) $L/D = 1.31$, (*b*) $L/D = 1.68$.

The velocity field in the rear corner region is shown in greater detail in figure 14(*a*, *b*). For $L/D = 1.31$, the time-averaged shear layer remains detached. Along the rear face of the cylinder, the mean flow moves upstream around the rear edge within the reverse flow region. On the other hand, the leading-edge shear layer reattaches shortly upstream of the rear corner of the $L/D = 1.68$ cylinder, and the flow leaving the trailing edge is nearly parallel to the sidewall of the cylinder. Note also the different size and position of the time-averaged vortex in the immediate wake of each cylinder in each case.

In figures 15 and 16, the velocity profiles are plotted from the velocity field data given above. In figure 15(*a*) it can be seen that the separated shear layer from the leading edge has not reattached before reaching the trailing edge. Here x_f is measured from the leading edge of the model while the coordinate x is referenced with respect to the trailing edge of the model. Immediately downstream of the model, figure 15(*b*) shows that at $x/D = 0.68$ the region is still in the reverse-flow zone. Over the

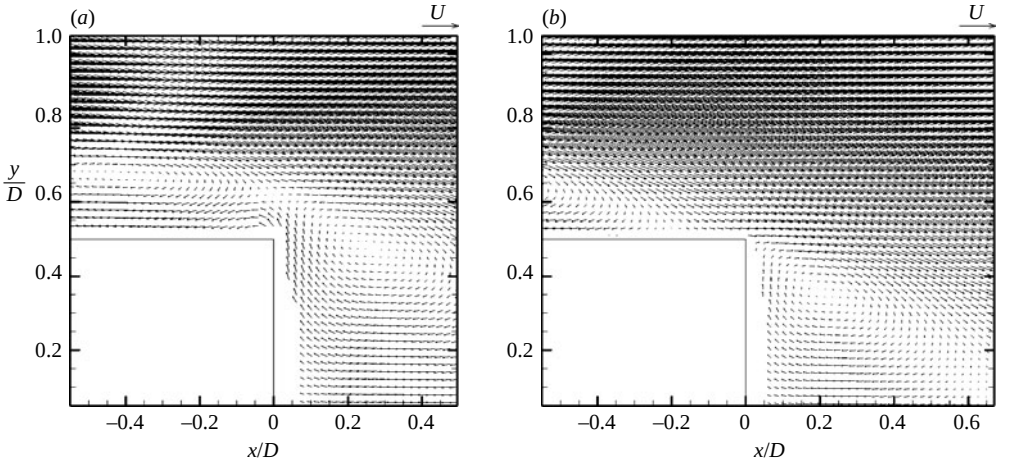

FIGURE 14. Mean velocity vector fields near the trailing edge ($Re_D = 1.0 \times 10^5$): (*a*) $L/D = 1.31$, (*b*) $L/D = 1.68$.

$L/D = 1.68$ model at $x/D = -0.18$ ($x_f/D = 1.5$ from the leading edge) (figure 16*a*), the separating shear layer has just reattached (note the reverse flow still at $x_f/D = 1.4$). At the trailing edge of the model, the boundary layer is just beginning to grow, but the spatial limitation of the PIV did not allow sufficient resolution within the boundary velocity profile. The station $x/D = 0.68$ is near the end of the reverse flow region (figure 16*b*). The drag due to the base pressure decreases with the wake size in the immediate wake as the fineness ratio increases (see figure 10). In contrast, it should be noted that with a fixed separation point, such as behind a disk (Bigger, Higuchi & Hall 2006), the smaller wake size signifies an increased base drag.

Ota (1975) used hot-wire anemometry on a rear-mounted cylindrical model. While its use in the vicinity of this type of separating flow may be suspect, the deduced streamlines and the location of the flow reattachment agreed well with the current PIV measurement. Using a split-film probe, Kiya *et al.* (1991) also found that the reattachment length over their long cylinder was 1.6 diameters. Koenig & Roshko (1985) placed a disk coaxially ahead of a similarly shaped flat-faced cylinder, and by varying the gap size and diameter ratio between the disk and the cylinder, they examined the flow pattern and its effect on the total drag. For the diameter ratio of 1, which is most analogous to the present case, they found that the separating shear layer attached to the front edge of the cylinder for gap sizes 1 and 1.625 (normalized by the cylinder diameter). The total drag was minimized for a similar gap size of 1.5, though the flow field below the shear layer was quite different due to the cavity. Furthermore, for a larger gap size the drag increase found in Koenig & Roshko (1985) was caused by the separated shear layer impinging on the front surface of the downstream cylinder, whereas in the present case, the drag increase for larger values of L/D was due to the boundary layer growth (see figures 6 and 8).

3.3.2. *Fluctuation flow field*

Representative instantaneous vorticity fields are plotted together with the instantaneous velocity vectors for two L/D in figure 17. Shear layer instability waves are visible along the separating shear layer and are nearly axisymmetric. Sigurdson (1995) was among the first to control shear layer vortices in this region by forcing these high-frequency instabilities to promote the growth of a large vortex structure near the

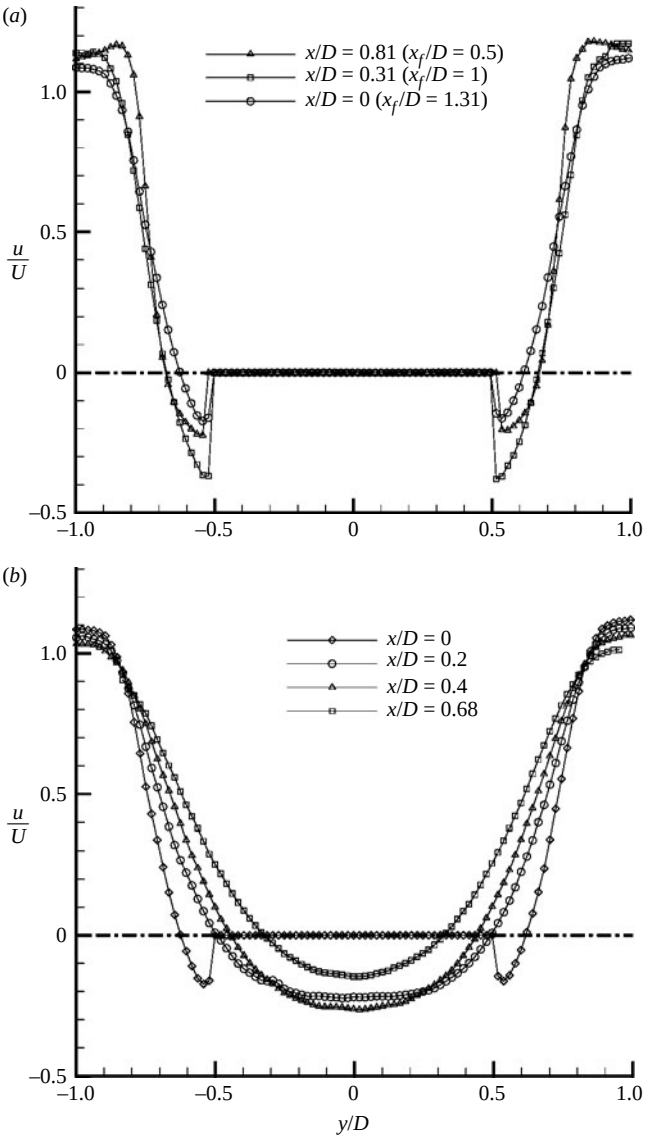

FIGURE 15. Mean velocity profiles over and behind $L/D = 1.31$ cylinder: (a) upstream: $x/D = -0.8 \sim 0$, (b) downstream: $x/D = 0$–0.68, x_f is measured from the leading edge of the model and x from the trailing edge.

trailing edge. Figure 17(a) shows the shear layer approaching the trailing edge without reattachment. The shear layer converges over the $L/D = 1.68$ model (figure 17b) with unsteady impingement of vortices on the surface. Note the asymmetric large structure near the trailing edge and the reattachment region in both cases. While the mean velocity field (see figure 12 from the same runs) indicates a well-defined closed separation bubble along the long cylinder, the instantaneous velocity field shows that the trailing edge of the shear layer is often open, with unsteady vortex structures impinging on the wall. Flow visualization in water also showed three-dimensional vortex ring structures impinging on the surface. Kiya *et al.* (1991) measured surface

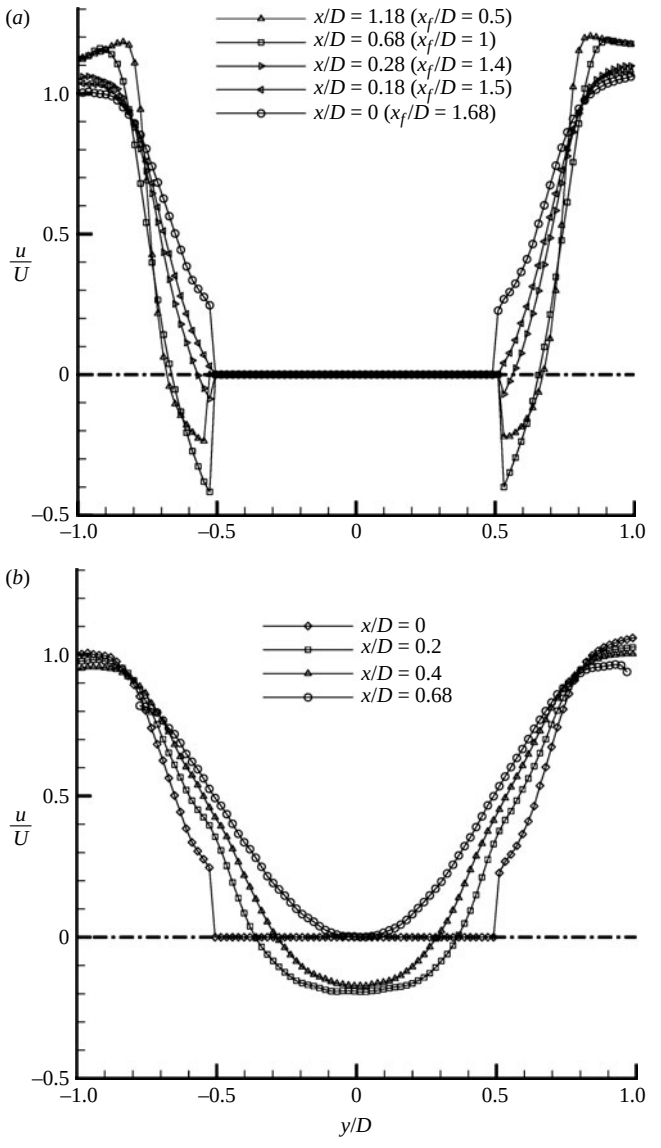

FIGURE 16. Mean velocity profiles over and behind $L/D = 1.68$ cylinder: (*a*) upstream: $x/D = -1.18$–0, (*b*) downstream: $x/D = 0$–0.68.

pressure fluctuations beneath the separation bubble over a blunt circular cylinder, and noted large-scale vortex shedding, as well as low-frequency shear layer oscillations. The former is attributed to the flow feedback within the separation bubble. The data rate of our PIV system did not allow contiguous time-dependent information, but shear layer instability waves and the large vortex formation downstream of $x/D \sim -1$, as well as the flapping of the reattaching shear layer itself, can be observed in figure 17. Time-dependent measurements of the base pressure and the force will be addressed in the next section.

In figure 18, the axial turbulence profiles are plotted radially at several stations and compared for two cylinder lengths, $L/D = 1.31$ and 1.68. These data have been

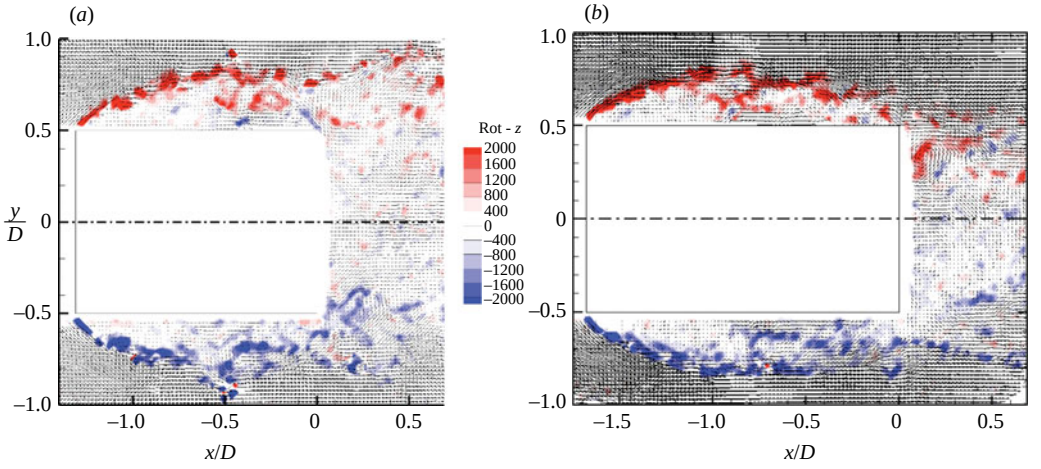

FIGURE 17. Instantaneous vorticity and velocity field: (*a*) $L/D = 1.31$ model, (*b*) $L/D = 1.68$ model (units of vorticity s^{-1}).

extracted from the PIV snapshots shown in figure 17. Here, the velocity component fluctuations in the (x, y, z) direction are denoted by (u', v', w'), respectively.

In this plot over the shorter cylinder ($L/D = 1.31$), a lower Reynolds number ($Re_D = 6 \times 10^4$) was chosen because of the overall consistency of data for that particular run with no change in flow pattern discernible between $Re_D = 6 \times 10^4$ and 10^5. The region $x_f/D = 1$ is where the large vortex structure was seen forming in the instantaneous flow field. Between $x_f/D = 1$ and the trailing-edge region, turbulence peaks over the $L/D = 1.68$ cylinder become weaker and closer together, reflecting the mean separation bubble streamline (see figure 13). In the wake region, the turbulence level is substantially reduced behind the $L/D = 1.68$ cylinder. Note that the turbulence intensity is higher at $x/D = 0.68$ than at $x/D = 0.4$. In the central region the intensity level approaches the bell-shaped profile due to interaction between the turbulence in the wake shear layer and the global wake oscillation across the centreline.

The azimuthal wake flow field was investigated in the cross-section normal to the free-stream direction. The instantaneous vorticity fields in the immediate wake are compared between two models at different downstream stations in figures 19 and 20. The instantaneous velocity field is overlaid in the figure. At 0.33 diameters downstream of the trailing edge, figure 19(*a*) shows a multitude of counter-rotating longitudinal vortices within the separating shear layer behind the short cylinder ($L/D = 1.31$), whereas behind the longer cylinder ($L/D = 1.68$, figure 19*b*) the vortical structures are more concentric. Kiya *et al.* (1991) noted a nine-cell structure in the shear layer reattachment region of a long cylinder by cross-correlating the circumferential surface pressure measurement at the same Reynolds number as the present experiment. Further downstream, the vortical structure and shear layer are highly asymmetrical behind the $L/D = 1.31$ cylinder (figure 20*a*), and, taken together with other snapshots, demonstrate the large three-dimensional excursion of the wake vortex motion. Behind the $L/D = 1.68$ cylinder (figure 20*b*), the intensity of the vorticity is reduced and the shear layer activity is limited to the region within the model diameter. As noted earlier, these PIV measurements could not identify the direction of the movement of the large structure.

Though the wake was highly asymmetrical and unsteady, when 2000 instantaneous velocity fields taken over 667 s were ensemble-averaged, remarkable flow symmetry

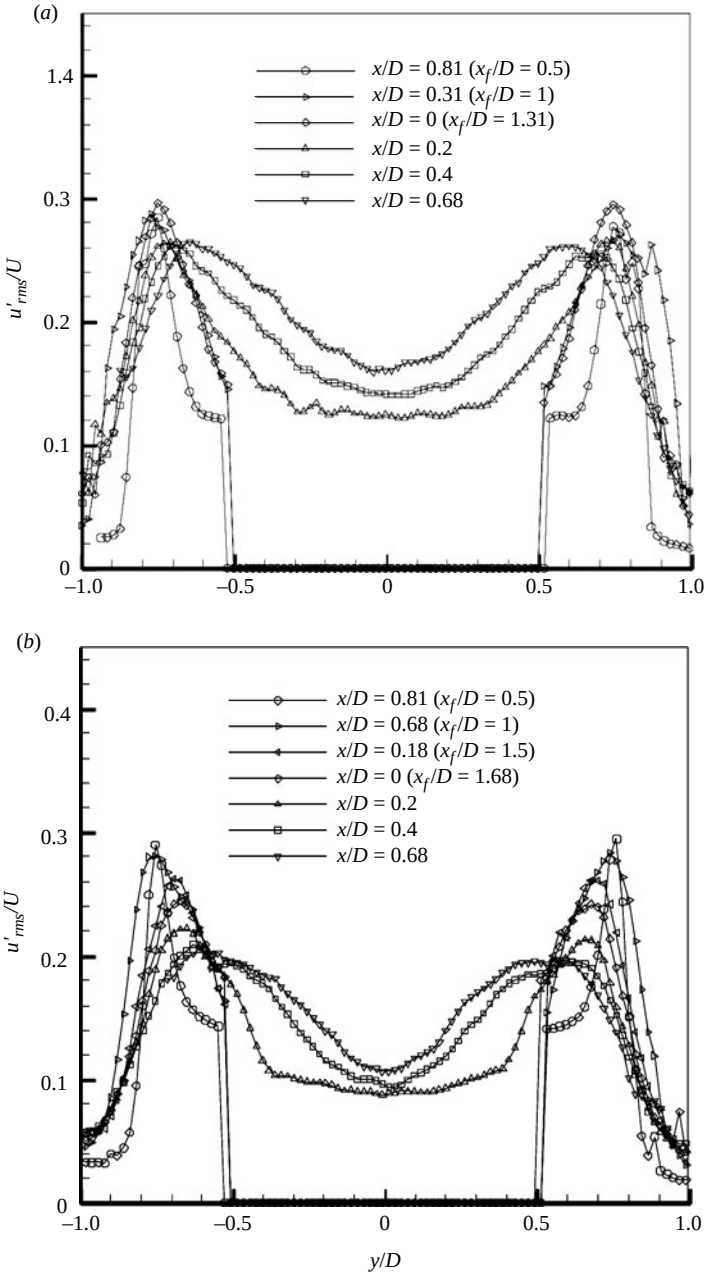

FIGURE 18. Axial turbulence profiles at various streamwise stations: (*a*) $L/D = 1.31$ model $Re_D = 6 \times 10^4$, (*b*) $L/D = 1.68$ Model $Re_D = 1.0 \times 10^5$.

emerged. Figure 21 shows the results for the $L/D = 1.33$ cylinder. The mean-square velocity fluctuation exhibited a torus-shaped profile immediately downstream of the cylinder (figure 21*a*). Further downstream at $x/D = 1.5$ (figure 21*b*) the ensemble-averaged turbulence profile becomes filled-in at the centre, approaching a Gaussian-like profile. The mean velocity vector was essentially normal to the measurement plane, subject to an increased uncertainty level. Despite a slight non-uniformity in the

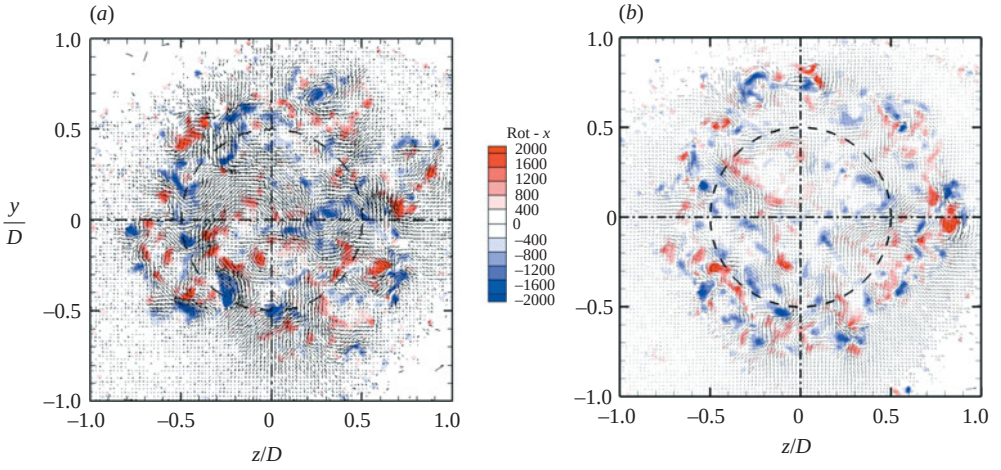

FIGURE 19. Instantaneous vorticity and velocity field in the cross-flow plane of the wake at $x/D = 0.33$ (units of vorticity s^{-1}): (*a*) $L/D = 1.31$, (*b*) $L/D = 1.68$.

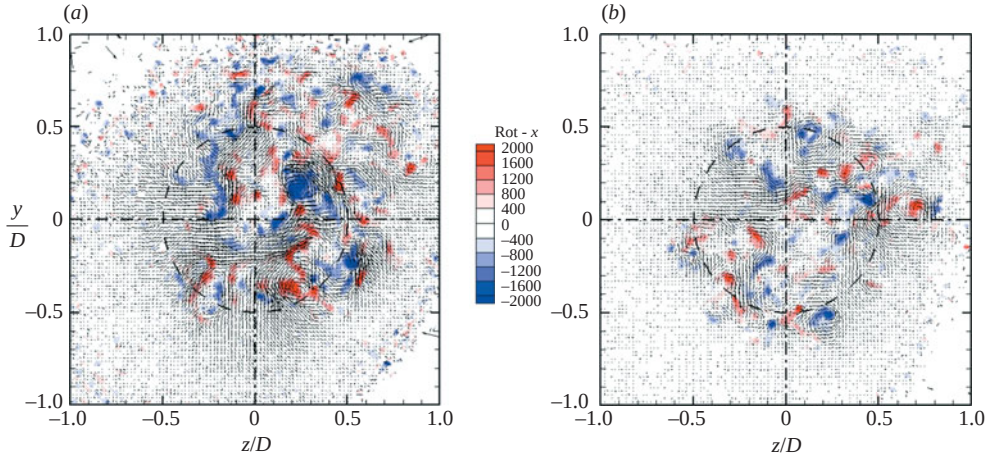

FIGURE 20. Instantaneous vorticity and velocity field in the cross-flow plane of the wake at $x/D = 1.5$ (units of vorticity s^{-1}): (*a*) $L/D = 1.31$, (*b*) $L/D = 1.68$.

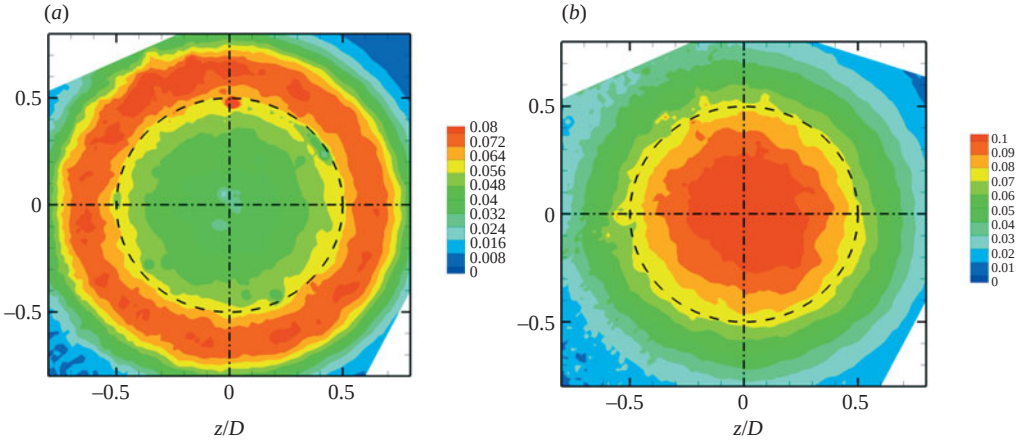

FIGURE 21. Ensemble-averaged mean-square turbulence distribution behind $L/D = 1.31$ model, $\overline{v'^2 + w'^2}/U^2$: (*a*) $x/D = 0.33$, (*b*) $x/D = 1.5$.

figure, however, the overall symmetry of the present results clearly demonstrates the merit of the magnetic support system over the sting-mounted model.

The present experiment was conducted with a low free-stream turbulence level. On the other hand, Roberson *et al.* (1972) used a free-stream turbulence level of up to 8 % to promote the shear layer reattachment at small fineness ratios. The effect of turbulence was prominent for the $L/D = 1$ case, which produced an earlier shear layer attachment accompanied by decreased overall drag. The base pressure coefficient was changed from approximately -0.3 to -0.1 due to the applied grid turbulence (compare with figure 9). Sigurdson (1995) and Kiya, Shimizu & Mochizuki (1997) directly forced the separating shear layer at the leading-edge shoulder of the long cylinder. The reattachment length could be shortened dramatically, or practically eliminated, depending on the forcing frequency and its amplitude. Amalgamation of shear layer vortices could be effective enough for them to impinge on the wall immediately after their roll-up (Sigurdson 1995). The present experimental focus was on the separated shear layer structure, and control of such separated shear layers with external forcing will be a future task. The axisymmetric and helical excitations of the disk wake have been examined in Bigger *et al.* (2006).

3.3.3. *Remarks on pressure and force fluctuation*

The present magnetic suspension and balance system monitored the instantaneous model position and the coil current needed to keep it in place through a feedback system. An example of the time history of the model position was shown in figure 3. Even though the model movement was small, it is possible to utilize this information further. The acceleration of the model is balanced by the aerodynamic force and the magnetic force as follows, given a position vector of the model $\boldsymbol{x}$ and the mass of the model m:

$$m\ddot{x} = F'_{aerodynamic} + F'_{magnetic}.$$

Here, the steady gravitational force vanishes. Because of the large mass ratio between the model and the working fluid, the virtual mass term is neglected. The position record was first low-pass filtered at 15 Hz before time-derivatives were taken in the light of the feedback system characteristic. Typical time histories of resulting magnetic force, inertia force and the drag are shown in figure 22. In this figure, the model coordinate system was used where the positive force is in the upstream direction. The RMS variation of the drag is approximately 7 % of the mean drag. The spectra of the drag and side force variations in figures 23 and 24, respectively, revealed a peak at $St \sim 0.081$ (10.4 Hz in the figure). Another peak at $St = 0.012$ (1.5 Hz) was observed in the drag time history but not in the side force. The base pressure data were also sampled at sufficiently high rate, and they exhibited a primary spectral peak at approximately $St = 0.34$ on the models in the range of $L/D = 1.27$ and 1.79. In addition, a very low-frequency oscillation corresponding to approximately $St = 0.012$–0.016 was observed for short models up to $L/D = 1.55$. This low-frequency oscillation, which was also observed in the axial aerodynamic force, is deemed to correspond to the axisymmetric pulsation of the recirculation bubble similar to that observed behind a thin disk at $St = 0.05$ by Berger, Scholz & Schumna (1990). Kiya *et al.* (1991) measured the surface pressure fluctuations in the region of the shear-layer reattachment, and observed that the shear layer flapping motion corresponded to $St = 0.4$ and 0.07 normalized with the cylinder diameter. These frequencies are close to the present spectral peaks at $St = 0.34$ and 0.10 observed in the base pressure and the aerodynamic force variations, respectively. Behind a thin

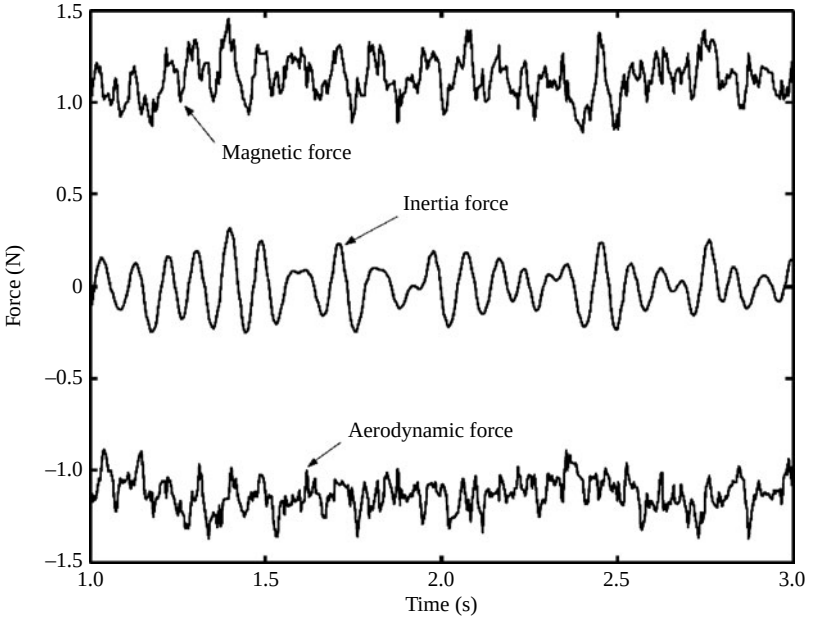

FIGURE 22. Drag, magnetic force and inertia force variation ($L/D = 1.27$, $Re_D = 1.0 \times 10^5$).

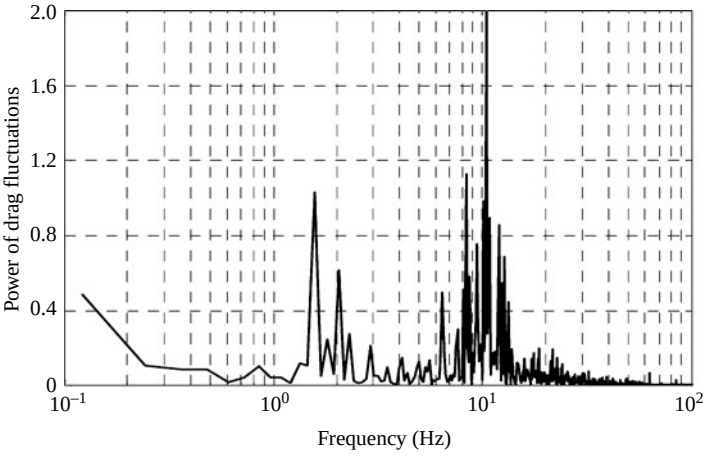

FIGURE 23. Power spectrum of drag force fluctuation ($L/D = 1.27$, $Re_D = 1.0 \times 10^5$).

disk, Berger *et al.* (1990) measured the shear layer instability waves at $St = 1.62$ and helical vortex shedding at $St = 0.135$. As stated earlier, the hot-wire measurement in the wake shear layer behind the $L/D = 5$ model showed the spectral peak at $St = 0.185$. Behind a thicker disk ($L/D = 0.125$), the the Strouhal number measured in water with a time-resolved PIV also increased to 0.15 (Bigger *et al.* 2006), and the present data appear consistent with the previous results. The present PIV data were taken at too large an interval to directly correlate the helical vortex shedding to the base pressure fluctuation. The frequency information of the present base pressure and force measurement warrants further examination, but it illustrates the unique capability of the experimental arrangement.

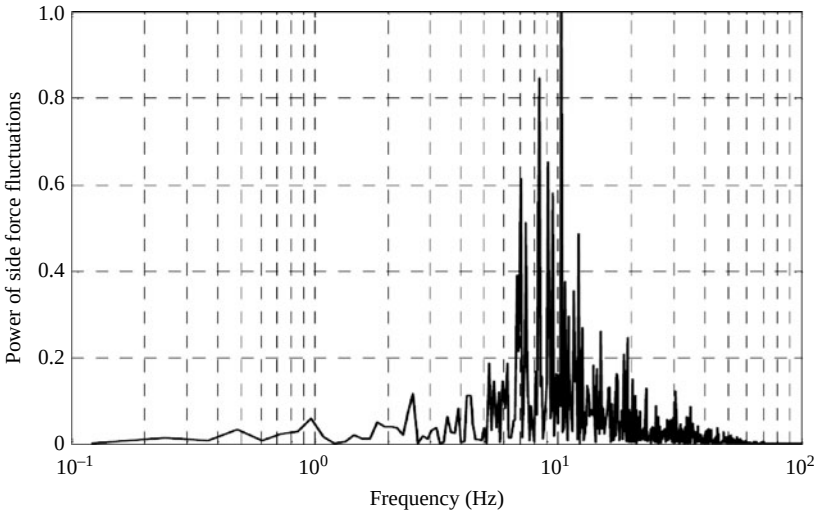

FIGURE 24. Power spectrum of side force fluctuation ($L/D = 1.27$, $Re_D = 1.0 \times 10^5$).

4. Conclusion

The drag coefficient variation of a right circular cylinder placed in an axial flow was obtained over a wide range of fineness ratio. In order to avoid flow interference with any model support and to ensure axisymmetry of the flow, the experiment was conducted using a magnetic suspension and balance system. The flow field in the wake and boundary layer, as well as the behaviour of the shear flow separated from the leading edge, was studied utilizing particle image velocimetry to corroborate complement the measured drag variation.

The minimum drag corresponded to the fineness ratio for which the separated shear layer reattached at the trailing edge, and at fineness ratios larger than approximately 1.7 the drag coefficient increased due to growth of the reattached boundary layer. The instantaneous velocity field around the cylinder, as well as in the wake, identified multi-level vortex structures. Unsteady large-scale longitudinal vortical structures travel across the entire wake behind a short cylinder but appear as organized axisymmetric torus-shaped turbulence energy profiles in the mean. Leading-edge shear layer vortices and downstream helical vortex structures were also observed. The variation in base pressure with fineness ratio measured via a telemetry system was consistent with the drag results. The measured base pressure fluctuation and aerodynamic force fluctuation were also examined.

This work was supported by the Grant-in-Aid for Scientific Research from the Japan Ministry of Education, Science and Culture. Authors acknowledge technical assistance of Mr Tetsuya Kunimasu during the experiment at JAXA. They also thank Drs Peter Simpkins and Joe Hall of Syracuse University for reading the manuscript.

REFERENCES

BEARMAN, P. W. & TRUEMAN, D. M. 1972 An investigation of the flow around rectangular cylinders. *Aeron. Q.* **23**, 229–237.

BERGER, E. SCHOLZ, D. & SCHUMM, M. 1990 Coherent vortex structures in the wake of a sphere and a circular disk at rest and under forced vibrations. *J. Fluids Struc.* **4**, 231–257.

Bigger, R., Higuchi, H. & Hall, J. W. 2006 Open-loop control of the disk wake in air and in water. *AIAA Paper* 2006-3187.

Blevins, R. D. 1984 *Applied Fluid Dynamics Handbook*, Van Nostrand Reinhold.

Crowe, C. T., Elger, D. F. & Roberson, J. A. 2005 *Engineering Fluid Mechanics*, 8th Edn. pp. 447–455. John Wiley & Sons.

Eiffel, G. 1907 *Recherches Expérimentales sur la Résistance de l'Air Exécutées à la Tour Eiffel*., L. Maretheux, Impimeur.

Eiffel, G. 1913 The resistance of the air and aviation (translated by J. C. Hunsaker). London: Constable Co., Boston: Houghton, Mifflin & Co.

Higuchi, H., van Langen, P., Sawada, H. & Tinney, C. E. 2006 Axial flow over a blunt circular cylinder with and without shear layer reattachment. *J. Fluids Struc.* **22**, 949–959.

Hoerner, S. F. 1958 *Fluid Dynamic Drag*, pp. 3–12. Published by author.

Judd, M., Vlajinac, M. & Covert, E. E. 1971 Sting-free drag measurements on ellipsoidal cylinders at transition Reynolds numbers. *J. Fluid Mech.* **48**, 353–364.

Kiya, M., Mochizuki, O., Tamura, H., Ishikawa, R. & Kushioka, K. 1991 Turbulence properties of an axisymmetric separation-and-reattaching flow. *AIAA J.* **29**, 936–941.

Kiya, M., Shimizu, M. & Mochizuki, O. 1997 Sinusoidal forcing of a turbulent separation bubble. *J. Fluid Mech.* **342**, 119–139.

Koenig, K. & Roshko, A. 1985 An experimental study of geometrical effects on the drag and flow field of two bluff bodies separated by a gap. *J. Fluid Mech.* **156**, 167–204.

Nakaguchi, H. 1978 Recent Japanese research on three-dimensional bluff-body flows relevant to road-vehicle aerodynamics. In *Aerodynamic Drag Mechanisms of Bluff Bodies and Road Vehicles* (ed. G. Sovran, *et al.*), pp. 227–246. Plenum.

Ohya, Y. 1994 Note on a discontinuous change in wake pattern for a rectangular cylinder. *J. Fluids Struct.* **8**, 325–330.

Ota, T. 1975 An axisymmetric separated and reattached flow on a longitudinal blunt circular cylinder. *J. of Appl. Mech.*, June 1975, pp. 311–315.

Pankhurst, R. C. & Holder, D. W. 1952 *Wind-Tunnel Technique*, Chapter 8. Sir Isaac Pitman & Sons.

Park, W.-C. & Higuchi, H. 1989 Computations of the flow past single and multiple bluff bodies by a vortex tracing method. *University of Minnesota Supercomputer Institute Rep.* UMSI 89/88.

Roberson, J. A., Lin, C. Y., Rutherford, G. S., & Stine, M. D. 1972 Turbulence effects on drag of sharp-edged bodies. *J. Hydraul. Div. ASCE*, 1187–1209.

Roos, F. W. & Willmarth, W. W. 1971 Some experimental results on sphere and disk drag. *AIAA J.* **9**, 285–291.

Sawada, H., Higuchi, H., Kunimasu, T. & Suda, S. 2004 Drag coefficients of cylinders magnetically suspended in axial flow. *J. Wind Engng* **29**, 55–62 (in Japanese).

Sawada, H. & Kunimasu, T. 2001 Status of MSBS study at NAL. 6th *Int. Symp. on Magnetic Suspension Technology, Oct. 7–11, Turin, Italy* (ed. G. Genta, H. Schneider-Muntau, L. di Gloria & W. Green), pp. 163–168. Politecnico di Torino.

Sawada, H., Kunimasu, T., Suda, S., Misunou, T. & Higuchi, H. 2005 Relation between base pressure and fineness ratio of axial cylinder. *37th Fluid Dynamics Conference, Sept. 15–16, Chiba, Japan* (in Japanese).

Schlichting, H. 1968 *Boundary layer theory*. McGraw-Hill.

Sigurdson, L. W. 1995 Structure and control of a turbulent reattaching flow. *J. Fluid Mech.* **298**, 139–165.

Watanabe, S. & Kato, H. 2003 Stereo PIV applications to large-scale low-speed wind tunnels. *AIAA Paper* 2003-0919.